

Blade Element Momentum Modeling of Low-*Re* Small UAS Electric Propulsion Systems

Matthew H. McCrink¹ and James W. Gregory²
The Ohio State University, Columbus, Ohio, 43235

A model for the propulsion system of a small-scale electric Unmanned Aircraft System (UAS) is presented. This model is based on a Blade Element Momentum (BEM) model of the propeller, with corrections for tip losses, Mach effects, three-dimensional flow components, and Reynolds scaling. Particular focus is placed on the estimation of scale effects not commonly encountered in the full-scale application of the BEM modeling method. Performance predictions are presented for geometries representative of several commercially available propellers. These predictions are then compared to experimental wind tunnel measurements of the propellers' performance. The experimental data supports the predictions of the proposed BEM model and points to the importance of scale effects on prediction of the overall system performance.

Nomenclature

a_0	=	axial inflow correction factor
a_1	=	radial inflow correction factor
A	=	test section area, m ²
B	=	number of blades
c	=	chord, m
C	=	faring area, m ²
C_D	=	drag coefficient
C_L	=	lift coefficient
$C_{L,pot}$	=	lift coefficient from potential flow theory
C_N	=	normal force coefficient
C_P	=	power coefficient
C_Q	=	torque coefficient
C_T	=	thrust coefficient
D	=	diameter, m
E	=	voltage, V
f	=	local Prandtl tip loss correction factor
F	=	Prandtl tip loss correction factor
I	=	current, A
J	=	advance ratio
K	=	local velocity correction factor
L	=	lift, N
M	=	Mach number
n	=	rotation rate, rev/sec
P	=	power, W

¹ Ph.D. candidate, Department of Mechanical and Aerospace Engineering, Aerospace Research Center, 2300 West Case Rd., AIAA Student Member.

² Associate Professor, Department of Mechanical and Aerospace Engineering, Aerospace Research Center, 2300 West Case Rd., AIAA Senior Member.

q	=	dynamic pressure, Pa
Q	=	torque, N-m
r	=	radius, m
Re	=	Reynolds number
T	=	thrust, N
V	=	velocity, m/s
V_l	=	local section velocity, m/s
V_r	=	radial velocity m/s
V_∞	=	freestream velocity, m/s
V_1	=	velocity across propeller disk, m/s
V_2	=	downstream velocity, m/s
Greek		
α	=	angle of attack
η	=	efficiency
θ	=	geometric angle of attack, rad
ϕ	=	Inflow angle
ρ	=	density, kg/m ³
σ	=	propeller solidity
τ	=	tunnel correction factor
ω	=	rotation rate, rad/s

I. Introduction and Background

DEVELOPMENT of a predictive propulsion model for small scale unmanned aerial systems (UAS) represents a continuing challenge for the designers of these vehicles. Typical components available for small scale UAS are not supported by robust performance data sets. This paper presents a predictive performance model for an electric propulsion system typically found on a small UASs. The model attempts to capture the effects of Reynolds scaling on the overall performance of the system at various operating conditions. The predictive model is based on the Blade Element Momentum (BEM) methodology, which has been widely used for full-scale wind turbines, helicopters and propellers¹⁻⁴. Several corrections to the basic model are needed to capture three-dimensional effects and are presented in section II.A.

The BEM modeling methodology has been applied to small-scale propeller testing by Uhlig and Selig⁴ to predict the performance at extreme angles of attack, but without handling Reynolds scaling effects. Several investigations report experimental data sets for small-scale UAS propellers,⁵⁻⁷ citing the lack of published performance information, but a comprehensive and accurate model of small-scale propeller and propulsion system performance is still lacking.

This work seeks to match the performance predictions of a BEM model to experimental data gathered on geometrically similar propellers over a range of Reynolds numbers. Emphasis is placed on the quantification of operational conditions and local Reynolds number effects on the overall propulsive efficiency. Reynolds effects are anticipated to be of first-order importance to the propeller performance. However, BEM models typically do not include Reynolds scaling effects, which is a key contribution of this work. By combining estimates of the electrical efficiency with the propeller efficiency, a model relating the measured electrical power to the thrust power can be developed. The results of the BEM model will allow for real-time estimation of the power available for flight testing operations. This model can be used with real-time measurements of airspeed, propeller rotation speed, and electrical power to infer the power supplied to the flow under various flight test conditions. This estimate is valuable for rapid flight test determination of the aircraft's drag polar and closed-loop control for real-time optimization of vehicle performance.

II. Blade Element Momentum Model

The Blade Element Momentum (BEM) model attempts to incorporate the geometric properties of the propeller system into a momentum transfer based model of the flow. Determination of the thrust and torque derives from individually analyzing small elemental sections along the span. In this work, data on elemental sections is generated computationally, creating a look-up table for input to the BEM model. The individual forces acting on each section are integrated to find the total force in the direction of motion, the thrust, and the torque opposing the rotation of the blade. Figure 1 shows the streamtube encapsulating the propeller and Figure 2 shows the basic forces acting on an elemental blade section.

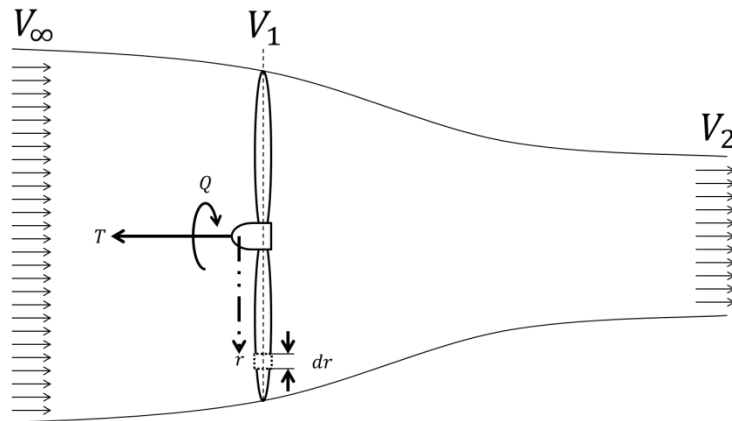


Figure 1: Farfield streamtube for BEM model development.

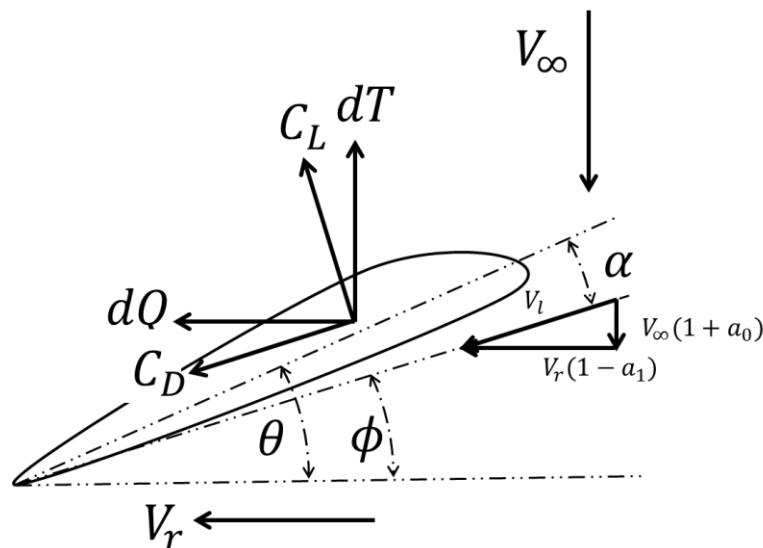


Figure 2: Local blade section properties for BEM model development. Forces and torques represent those acting on an infinitesimal blade element.

The differential thrust and torque forces are integrated over the surface of the blade to determine the total force and torque produced by the propeller. A detailed derivation of the BEM model can be found in Madsen *et al.*¹ A basic overview of the BEM as applies to the proposed model is presented here. The primary difficulty in BEM modelling is the estimation of the induced axial and radial velocity components created by the rotating propeller. As the propeller is operating in a predominantly subsonic regime, the pressure field created by the propeller induces a rotational flow component upstream of the blade. The magnitude and direction of the induced velocity components vary in the spanwise direction as a function of the propeller's aerodynamic, geometric, and operational conditions. To date, there is no closed form solution for the induction factors. Therefore, an iterative approach is used to approximate them over a finite section of the propeller blade. The induced velocity factors, a_0 and a_1 are formulated by equating the local aerodynamic forces acting on the blade with the bulk momentum transfer of the blade to the streamtube surrounding the propeller. The thrust and torque components acting on each blade element are given by

$$\begin{aligned} dT &= \frac{1}{2} \rho V_\infty^2 cB \frac{(1+a_0)^2}{\sin^2 \phi} C_T dr \\ dQ &= \frac{1}{2} \rho V_\infty cB \omega r^2 \frac{(1+a_0)(1-a_1)}{\sin \phi \cos \phi} C_Q dr \end{aligned} \quad (1)$$

where C_T and C_Q are related to the local lift and drag coefficients by the rotation matrix given as

$$\begin{bmatrix} C_T \\ C_Q \end{bmatrix} = \begin{bmatrix} \cos \phi & -\sin \phi \\ \sin \phi & \cos \phi \end{bmatrix} \begin{bmatrix} C_L \\ C_D \end{bmatrix}. \quad (2)$$

From Figure 1, the total thrust can be determined via momentum balance between the upstream farfield and a location far downstream (shown as location 2 in Figure 1). Applying the conservation of momentum to the streamtube gives the following relationship for the thrust and torque components across the propeller disk

$$\begin{aligned} dT &= 4\pi r \rho V_\infty^2 (1+a_0)a_0 dr \\ dQ &= 4\pi r^3 \rho V_\infty \omega (1+a_0)a_1 dr \end{aligned} \quad (3)$$

Equating (3) with the geometric thrust and torque terms in (1) gives the following implicit relationship between the induced velocity components,

$$\begin{aligned} a_0 &= \frac{1}{\frac{4 \sin^2 \phi}{\sigma C_T} - 1} \\ a_1 &= \frac{1}{\frac{4 \sin \phi \cos \phi}{\sigma C_Q} + 1} \end{aligned} \quad (4)$$

where σ is the local solidity of the disk, given as the ratio of the local chord divided by the area of the annular disk formed by the infinitesimal radial blade element, $cB/2\pi r$.⁸⁻⁹ Using the relations provided by (3) and (4), an implicit iterative solver can be setup to approximate the axial and radial induction factors.

A. Corrections

The BEM model is nominally a 2-D estimation of local blade performance and therefore provides no connection between adjacent infinitesimal blade elements. For blades of moderate aspect ratio, there will be an appreciable spanwise variation in velocity, angle of attack, and Reynolds number. Radial flow components can dramatically affect the propulsive efficiency of the propeller.³ To account for the spanwise aerodynamic coupling, correction factors are introduced. These include allowances for tip losses, Mach effects, and pressure based radial flow components. The following sections detail these corrections.

1. Tip Loss Factor

The lift goes to zero as the radial location approaches the tip due to pressure equalization. Prandtl addressed this effect by incorporation of a tip loss coefficient.¹⁰ The tip loss factor is given as

$$F = \left(\frac{2}{\pi} \right) \cos^{-1} \left(e^{-f} \right), \quad (5)$$

and the localized correction factor f is given by

$$f = \frac{B}{2} \left(\frac{1-r}{r\phi} \right), \quad (6)$$

where B is the number of blades, and ϕ is the local inflow angle. The localized correction factor is a function of the blade inflow angle, which is determined iteratively in the BEM algorithm. These corrections represent a reduction in lift occurring near the tip of a blade element due to pressure equalization. The tip loss coefficient is incorporated into the BEM model by modifying the inflow coefficients a_0 and a_1 ,⁹

$$a_0 = \frac{1}{\frac{F 4 \sin^2 \phi}{\sigma C_t} - 1}, \quad (7)$$

$$a_1 = \frac{1}{\frac{F 4 \sin \phi \cos \phi}{\sigma C_q} + 1}.$$

2. Mach Number Correction

The tip Mach number on low pitch propellers can reach up to 0.6. At these Mach numbers, the 2-D airfoil sections will experience an increase in the lift curve slope approximated by Glauert's Mach correction factor,⁸ given as

$$C_L = \frac{C_{L, M=0}}{\sqrt{1-M^2}}. \quad (8)$$

The Mach correction is applied to the lift coefficient and drag coefficient for the cases considered in this work.

3. Three-Dimensional Flow Correction

Blade element momentum theory fundamentally assumes quasi two-dimensional flow, with no interaction between adjacent radial locations. However, spanwise flows are often present and cannot be accounted for with the baseline BEM technique. Thus, a semi-empirical correction must be used to address three-dimensional flow effects induced by the rotation of the blade.^{3,11,12} The correction model used in this work follows the work of Snel *et al.*³ and Liu & Janajreh,¹² and will be briefly summarized here within the context of propeller performance. The basic BEM model assumes that the blade sections are decoupled in the spanwise direction. Spanwise (radial) flows occur due to the presence of locally separated regions near the training edge which extend over some portion of the blade's surface. The complex pressure field resulting from these separated regions promotes a radial flow component which tends to move from root to tip, since the spanwise pressure gradient is stronger than the chordwise gradient in these separated regions. The bulk movement of fluid requires additional energy from the motor. The additional energy is formulated similarly to a mechanical pumping loss term. Semi-empirical corrections for the "pumping" loss were proposed by Snel *et al.* and Liu & Janajreh after detailed theoretical, computational, and experimental investigations. The correction relies on modification of the local lift coefficient based on its angle of attack and proximity to other stalled blade regions.

A reduction in the radial flow component occurs near the tip due to a lower angle of attack and localized pressure equalization. To match the extents of the three-dimensional effects, the centrifugal pumping correction is applied between the root and 85% of the span.³ The semi-empirical 3-D correction is formulated by augmenting the uncorrected 2-D normal force components, given by

$$C_{N_{3-D}} = C_{N_{2-D}} + 1.5 \left(\frac{c}{r} \right)^2 \left(C_{L, pot} - C_{L_{2-D}} \right) \left(\frac{\omega r}{V_l} \right)^2. \quad (9)$$

where the normal force coefficient is normal to the local airfoil chord. $C_{L,pot}$ is the lift coefficient from thin airfoil theory (potential flow) for a symmetric section evaluated at the local angle of attack. Estimation of the aerodynamic parameters required for the BEM and correction factors are addressed in the next section.

B. Geometric and Aerodynamic Parameters

1. Aerodynamic Coefficients

The coefficients for the BEM studies were generated using XFOIL and augmented with experimental data from Ostowari and Naik.¹³ XFOIL is a panel code designed to model the effects of viscosity (to first order), and hence Reynolds number on various aerodynamic bodies.¹⁴ The propellers evaluated in this work (made by APC) use the Clark Y airfoil section from 0 to 5% span, and the NACA 4412 for the remainder of the span. XFOIL was used to analyze 2-D sections over a range of Reynolds numbers from 10^4 to 10^6 , and angles of attack from -10 to 20 degrees in 0.5 degree increments (see Figures 3 and 4).

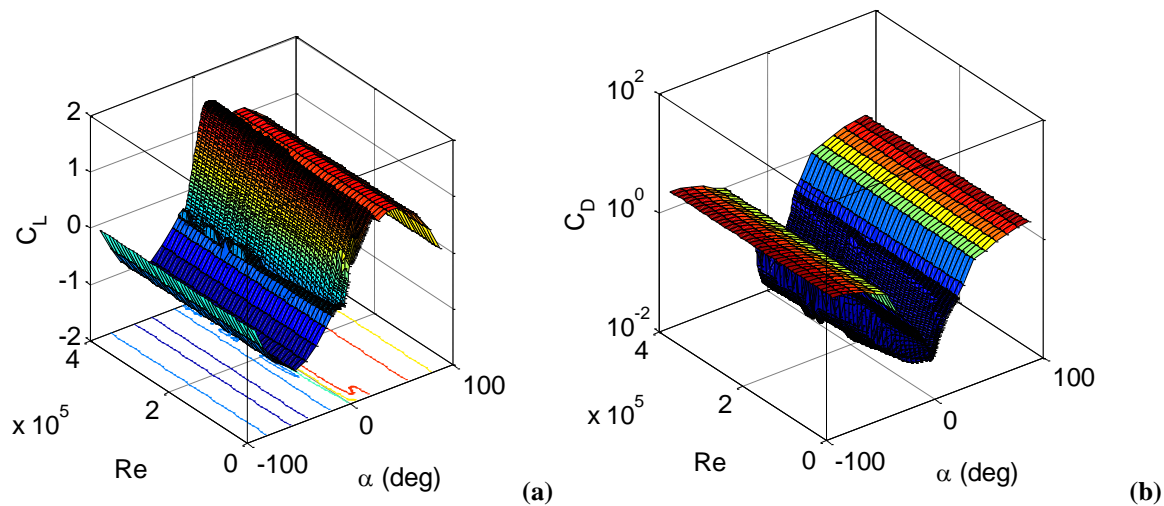


Figure 3: Lift (a) and drag (b) coefficients versus angle of attack and Reynolds number for NACA 4412.

For angles of attack beyond stall, high-alpha data from Ostowari and Naik's wind tunnel testing is used.¹³ The data covers the range of -10 to 110 degrees angle of attack. Studies on similar NACA sections provide the lift and drag data between -90 and -10 degrees.¹⁵ Representative results for a NACA 4412 operating at a Reynolds number of $100,000$ are shown in Figure 4. From this data set, local section coefficients are evaluated using MATLAB's polynomial interpolation functions.

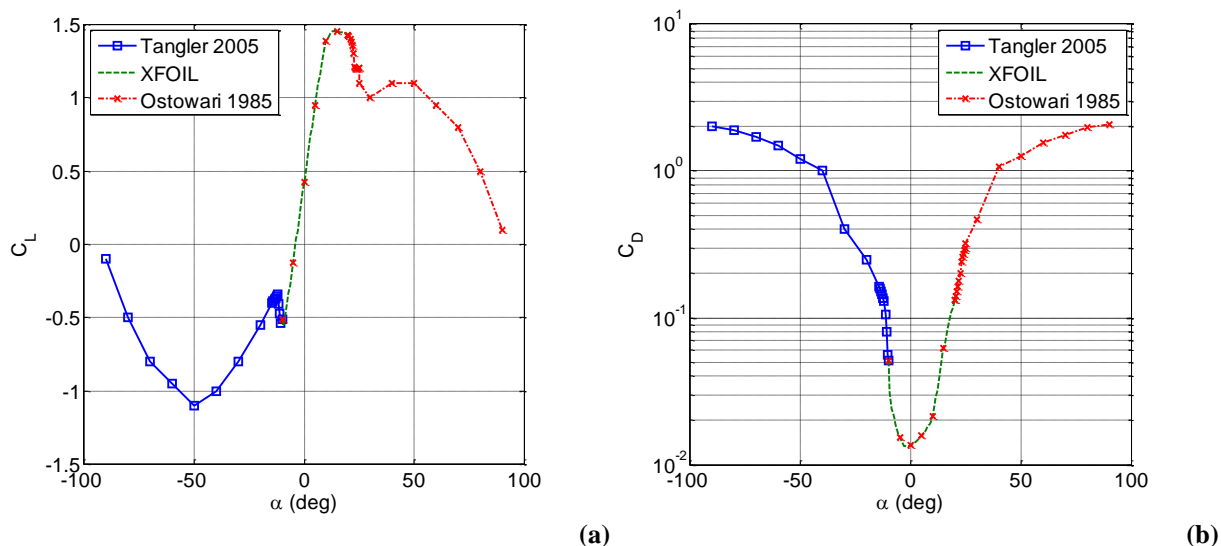


Figure 4: C_L (a) and C_D (b) for NACA 4412 at $Re = 100,000$.

2. Propeller Geometry Estimation

The APC propellers used for experimental ground and flight-testing were designed for a constant C_L across the majority of the blade section. This makes quantifying the exact spanwise chord and geometric angle of attack difficult. Thus, a visual integration method was developed in order to determine the blade geometry. The integration method correlates two perpendicular images to estimate the spanwise variation of chord and angle of attack. A third perpendicular image is used in difficult to resolve regions, typically occurring near the root and tip. The specific propellers investigated with the BEM are the APC 10×5, 10×6, and 10×7. The first number in the nomenclature represents the diameter of the blade (in inches). The second number represents the theoretical forward advance in one revolution of the blade (again, in inches).



Figure 5: Top view of APC 10×5, 10×6, and 10×7 propellers, from top to bottom.



Figure 6: Side view of APC 10x5, 10x6, and 10x7 propellers, from top to bottom.

For each propeller, two perpendicular images were collected. The first is in the streamwise direction allowing for identification of the hub region. The hub contains known feature sizes which create scaling and rotation datums. The second image is perpendicular to the streamwise direction and span. Figures 5 and 6 show representative images for each blade. The images were collected with a 10 MP Cannon DSLR camera, giving an effective resolution of 0.1 mm. From these images, negatives were formed using the edge detection and correction capabilities of the GIMP image editing software package, the results of which are shown in Figure 7. The negative images were derotated and scaled using MATLAB's image processing toolbox. Scaling relies on correlating known dimensions with pixel counts. The images taken in the streamwise direction show the hub and mounting hole which are of known size. After scaling based on hub size, the blade is derotated based on a known overall blade length.

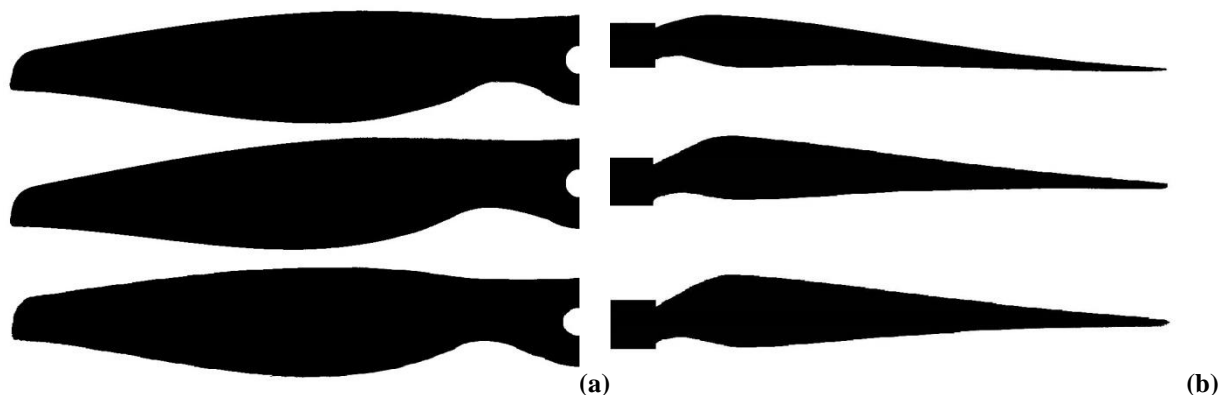


Figure 7: APC propeller top (a) and side (b) negative images

Alignment and registration of the top and side negatives occurs by finding the maximum cross-correlation between the top and side images. The chord is estimated by integrating the pixel count in the streamwise direction across the top image and the chordwise direction of the side image. The local chord is then the square root of the sum of the square of the top and side lengths estimated by pixel integration. The inverse tangent of the top and side pixel integral values gives the geometric angle of attack. Figure 8 shows the resulting angle of attack and chord variation for the blades used in this work. The BEM calculations start immediately outside the hub region. The hub is shown in Figure 8 and included only for clarity.

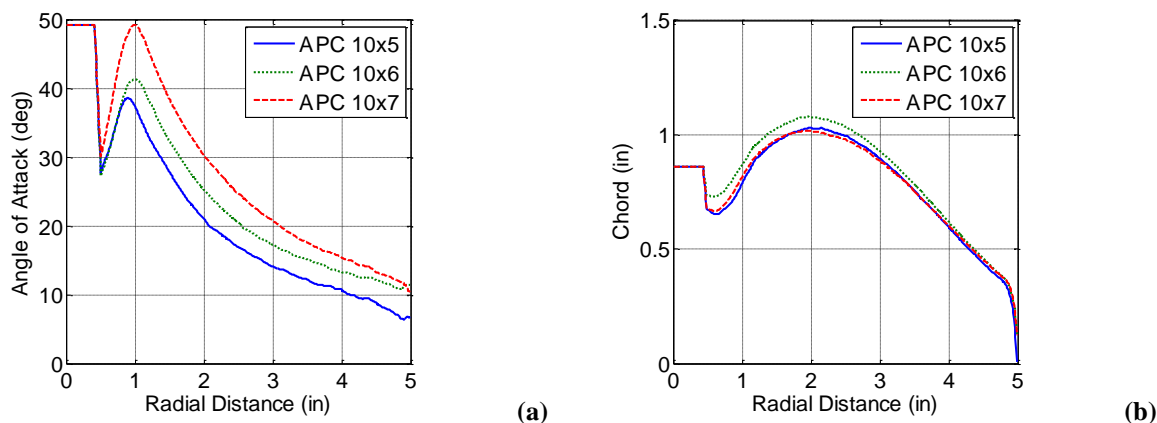


Figure 8: Angle of attack (a) and chord length (b) for APC 10x5, 10x6, and 10x7 propellers.

The propeller geometry was verified using a NextEngine 3-D scanner. This system generates a precise map of three-dimensional surfaces. However, it is unable to map the underside of the propeller. The accuracy of the sensor is limited to 0.5 mm with an overall point spacing of 2 mm. The results are a coarse estimate of the propeller geometry bounding the estimates provided by the imaging technique previously outlined. A representative dataset for the APC 10x6 is shown in Figure 9, which confirms the validity of the imaging technique.

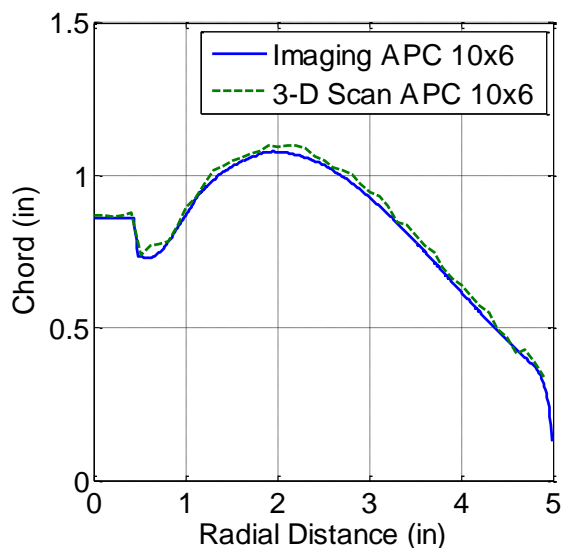


Figure 9: APC 10x6 chord distribution estimated by imaging and 3-D scan.

III. Blade Element Momentum Model Performance Predictions

A. Propeller Performance Metrics

This section details the terminology and metrics associated with the analysis of the propeller-based propulsion system. These include the non-dimensional parameters commonly associated with propeller design such as the advance ratio, thrust and power coefficients, and the propulsive efficiency.

1. Advance Ratio

The advance ratio is a dimensionless term used to quantify the effects of forward motion and angular velocity and is given as

$$J = \frac{V_{\infty}}{nD}, \quad (10)$$

where J is the advance ratio, n is the rotational frequency in rev/s, and D is the diameter of the propeller. For the fixed pitch propellers tested in this work, the angular velocity of the propeller is not constant. Instead, at high advance ratios, the decreasing angle of attack results in a drag reduction. The drag reduction decreases the power required to drive the propeller, resulting in a higher rotational velocity.¹⁶

2. Thrust, Torque, and Power Coefficients

The thrust and power coefficients are non-dimensional quantities relating the thrust and power producing capability of a propeller to its rotational velocity and diameter. From dimensional analysis, the thrust coefficient is given as

$$C_T = \frac{T}{\rho n^2 D^4}, \quad (11)$$

where T is the thrust, ρ the freestream density, n the rotation rate of the propeller, and D is the diameter. Following a similar development, the torque coefficient is expressed as

$$C_Q = \frac{Q}{\rho n^2 D^5}, \quad (12)$$

and the power coefficient as

$$C_P = \frac{P}{\rho n^3 D^5}, \quad (13)$$

where Q is the torque and P is the motor power required to drive the propeller.⁹

3. Propulsive and System Efficiencies

The propulsive efficiency is given as the ratio of the power transferred to the air mass moving through the propeller disk to the mechanical power required to drive the propeller. This is expressed as

$$\eta_{propulsive} = \frac{TV_{\infty}}{2\pi nQ} = \frac{1}{2\pi} \frac{C_T}{C_Q} J. \quad (14)$$

The propulsive efficiency is a key metric for comparison of propellers of different geometric configurations or operational conditions. For the electrical propulsion system used in this work, there is an additional electrical efficiency term used to correlate the electrical power delivered from the battery to the mechanical power produced by the motor. This efficiency term is given by

$$\eta_{electrical} = \frac{2\pi nQ}{EI}, \quad (15)$$

where E is the battery voltage and I is the supplied current to the electronic speed controller. In practice, the speed controller and motor efficiencies are lumped into a single term. The total system efficiency, a ratio of flow power to supplied electrical power, is therefore the product of the electrical and propulsive efficiencies:

$$\eta_{total} = \eta_{electrical} \eta_{propulsive}. \quad (16)$$

B. Operating Conditions

The BEM was applied to three propeller geometries as outlined in section II. The performance of each propeller was modeled over a range of advance ratios and Reynolds numbers, the limits of which were selected from previous flight and wind tunnel testing of the propulsion system and are summarized in Table 1. The overall goal of this work is to develop a linearized model which can be used for the inflight prediction of the power available. Limitations on the inflight power system restrict the model to conditions in which positive thrust is being produced. If the thrust drops below zero, the motor is extracting power from the freestream and the data provided by the onboard electrical system is no longer valid. Therefore, the BEM model was used with each propeller until a condition of zero thrust was reached.

Table 1: BEM operational bounds.

Parameter	Minimum	Maximum
J	0.01	1
n	4000 RPM	15,000 RPM
V_∞	0.01 m/s	45 m/s

C. BEM Thrust, Torque, and Power Coefficients

Figure 10 shows the BEM predicted thrust coefficient for the APC 10×5, 10×6, and 10×7. From Figure 10, the thrust decreases parabolically with increasing advance ratio. The parabolic relationship between thrust coefficient and advance ratio is common to small-scale fixed pitch propellers.⁵⁻⁷ Figure 11 shows the power coefficient for the three tested propellers. The magnitude and trending of the data is consistent with the published literature.⁵⁻⁶

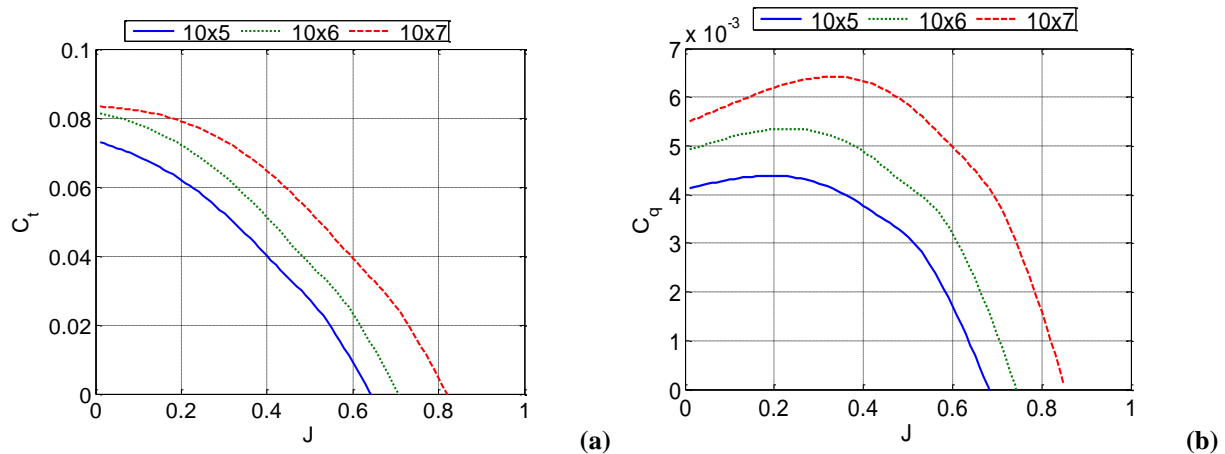


Figure 10: Thrust coefficient, C_T , (a) and torque coefficient, C_Q , (b) for APC 10×5, 10×6, and 10×7 propellers at 10,000 RPM.

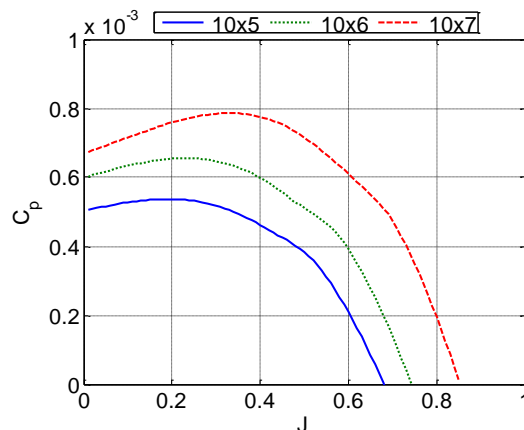


Figure 11: Power coefficient, C_p , for APC 10x5, 10x6, and 10x7 propellers at 10,000 RPM.

D. Propulsive Efficiency versus Advance Ratio

The propulsive efficiency is the key metric for inferring the power available in flight. Estimating the advance ratio is relatively straightforward as only the airspeed and motor RPM needs to be recorded. Determining the propulsive efficiency however, requires a correlation between the measured electrical power and the power delivered by the motor to the freestream as outlined in section III.A.3. Estimating the system efficiency is further complicated by a strong coupling between the thrust and propeller Reynolds number. Quantifying the propulsive efficiency versus propeller Reynolds number and advance ratio will allow for an approximation of the total system efficiency necessary to determine the power available in flight.

Figure 12 shows the BEM prediction of the propulsive efficiency for the three propellers considered in this work. From the BEM predictions, the theoretical advance of the propeller can be determined by finding the upper advance ratio limit at which the efficiency is zero. When the efficiency is zero, the propeller is essentially acting as an airscrew and the advance per revolution is equal to the advance ratio multiplied by the diameter of the propeller. Table 2 summarizes the BEM theoretical advance ratios from Figure 12. Others have noted the large discrepancy between published and measured advance. The performance variation is more dramatic when comparing propellers of the same diameter and advance from different manufacturers.^{5,6,18}

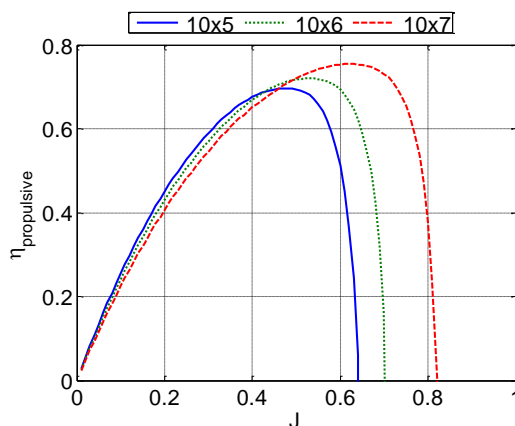


Figure 12: Propulsive efficiency, $\eta_{propulsive}$, versus advance ratio for the APC 10x5, 10x6, and 10x7 propeller at 10,000 RPM.

IV. Experimental testing

For the aircraft tested in this work, the thrust cannot be directly measured in flight. Therefore, a ground based assessment of the thrust and power performance is required for accurate determination of $\eta_{propulsive}$ and C_T in flight. These motor performance characteristics will be used to infer the inflight thrust at a measured advance ratio. Hobby

grade motor and propeller components commonly used on small UAS often lack sufficient quantitative thrust and power data.¹⁸ Therefore, a successive buildup method is proposed to quantify the individual component efficiencies as outlined in the previous sections. A test stand in a wind tunnel was used for measurement of the thrust and torque over a range of airspeeds and motor speeds in order to generate a map of propeller efficiency versus advance ratio. In addition to the thrust and torque data, engine RPM, motor voltage, and current were monitored. Figure 13 shows a schematic of the engine testing apparatus.

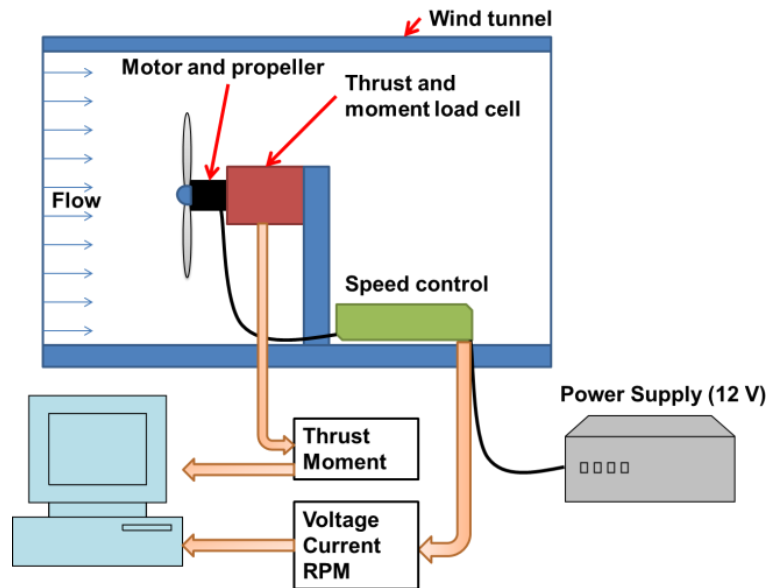


Figure 13: Schematic of propulsion system test setup.

A. Experimental setup

The thrust and torque measurements were made using a Futek MBA500 with a thrust rating of 222 N and a torque capacity of 5.64 N-m. RPM measurements were made using the back EMF produced by the commutating motor. The back EMF measurement technique produced a voltage spike each time the coils in the motor energized. The voltage spike passed through a Schmitt trigger providing a square wave output proportional to the motor RPM with six pulses per revolution. An inline Allegro ACS758 100-A current sensor allowed for measurement of the electrical power. A bank of six HP Proliant 406421-001 1300-W, 12-V server power supplies provided the electrical power necessary to run the motor. Each power supply was capable of providing 40 A and was placed in parallel to buffer the current output capability.

The wind tunnel is an open return type with a 22"×22" test section area. The tunnel has a maximum velocity of 65 m/s. The tunnel features a 3" flow straightening honeycomb structure on the inlet, followed by three turbulence-reducing screens. Tunnel velocity was measured using two static rings, with one placed in the plenum after the turbulence screens, and the other immediately before the test section. Test section dynamic pressure was measured across the two static rings using an Omega PX2650 differential pressure transducer. The test section is sealed; therefore, the local static pressure was recorded before and after the test section to account for variations in density and buoyancy effects. Test section static pressure was measured using two Omega PX2650 differential pressure transducers. The static temperature was measured near the test article using a K-type thermocouple and a National Instruments NI-9213 thermocouple amplifier. A model following controller designed in LabView controls the wind tunnel velocity. The controller allows for fast ramping and precise control over the test section velocity.

The RPM, current, voltage, torque, and thrust signals were sampled using a National Instruments NI-6009 data acquisition board. The DAQ gathers analog and digital information from all sensors at 10 kHz. The sampling rate was sufficiently higher than the vibrational modes of the thrust stand (2 kHz), which limited aliasing and allowed for adaptive filtering in the data reduction. The motor was mounted directly to the load cell for force and torque measurement, and the motor/load cell assembly was positioned in the center of the test section on a faired mount. A vibration isolation mount held the motor and increased the natural resonant frequency of the motor/propeller combination beyond the upper RPM limit. The vibration mount made the calibration of the thrust and torque sensor

more difficult by introducing elasticity into the system. However, the calibrations were repeatable over the course of the experimental campaign.

B. Wind Tunnel Correction Factors

Two correction factors were used to account for the influence of the wind tunnel on the performance of the system. The first accounts for the tunnel wall effects which can increase the static pressure in the propeller wake.¹⁹ Following the work of Barlow *et al.*¹⁹ and Brandt and Selig,⁵ the following corrected velocity is used in place of the measured tunnel velocity,

$$\frac{V_{\infty, \text{corr}}}{V_{\infty}} = 1 - \frac{TA/qC}{2\sqrt{1+2(T/q)}}. \quad (17)$$

The second correction addresses the local velocity increase caused by the presence of a three dimensional body in the wind tunnel (blockage). To correct the artificial increase in velocity, the method proposed by Brandt and Selig was used.⁵ Briefly, the increase in velocity is related to the relative volume of the test piece and the overall wind tunnel geometry. The relationship for the relative increase in velocity is given by¹⁹

$$\frac{V_{\infty, \text{corr}}}{V_{\infty}} = \frac{K\tau\psi}{A^{3/2}}, \quad (18)$$

where $K = 1.045$, $\tau = 0.92$, and the volume of the fairing (ψ) is 200 in^3 .

C. Full Power Performance

The experimental testing was divided into three sections. The first section focused on the full power testing of the propulsion system. For a fixed pitch blade, the increase in freestream velocity reduces the motor torque requirement via a reduction in blade angle of attack. This in turn allows the motor to rotate at a higher RPM. An increase in RPM varies the local Reynolds number and tip Mach number in a parabolic fashion. Testing at full power represents the upper performance limit for propeller, and an upper bound for the mapping between $\eta_{\text{propulsive}}$, J , and the Reynolds number.

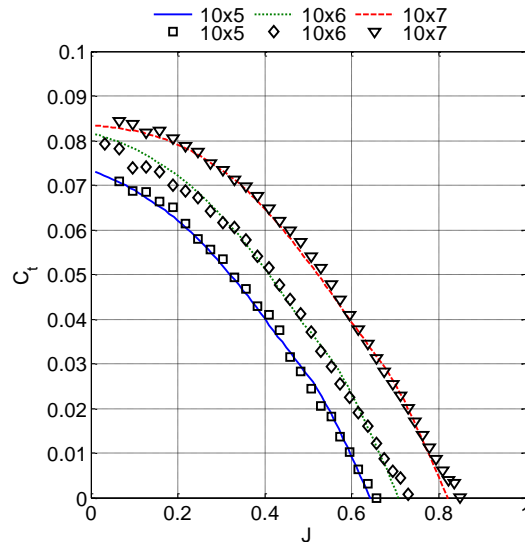


Figure 14: Analytic and experimental thrust coefficients for the APC 10x5, 10x6, and 10x7.

Figure 14 shows the BEM results for the predicted and measured thrust coefficient. From this plot, the overall trending from the BEM matches with the experimental data generated by the APC 10×5, 10×6, and 10×7 propellers. From the definition of the thrust coefficient, the close agreement is directly related to the accurate prediction of the thrust. For the given blade geometries, the thrust prediction is largely dependent on the fidelity of the local lift coefficient estimates. Within the advance ratios considered, the lift coefficient varies appreciably from -1 to 1.25 with an angle of attack variation between -30 and 25 degrees, as shown in Figure 15.

It should be noted that the results presented are sensitive to the characteristics of the blade section used, as shown in Figure 16. In this test, an APC 10×6 propeller shown with a geometrically similar 10×6 propeller using a NACA 0012 as the airfoil section. As the propeller geometry is similar, the section properties directly determine the difference in performance.

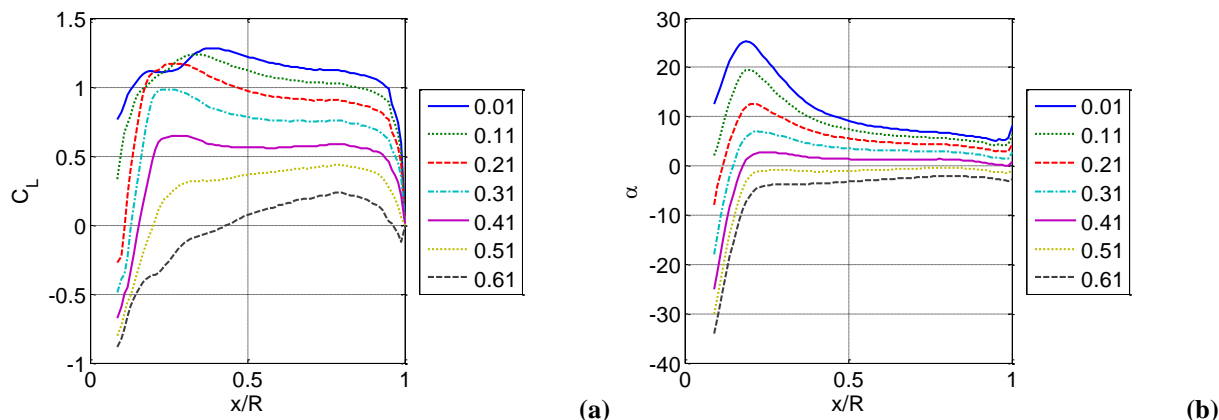


Figure 15: Spanwise C_L (a) and angle of attack (b) variation at different advance ratios for APC 10×5.

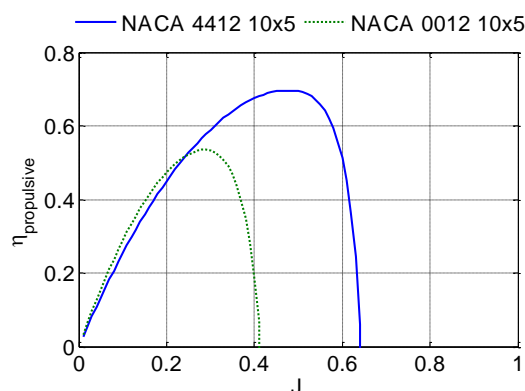


Figure 16: Performance variation for geometrically similar propellers with different airfoil sections.

The torque coefficient is shown in Figure 17. The trending at low advance ratios for the APC 10×7 is likely due to the angle of attack being beyond stall over the majority of the blade. In this condition, the predicted torque is sensitive to the magnitude of the drag coefficient as it increases parabolically with angle of attack. At low advance ratios, the inboard sections of the blade are stalled as shown in Figure 18. These stalled regions largely govern the required torque. As the advance ratio is increased, the torque required is relatively constant until the propeller angle of attack drops below the stall angle. Below the stall angle, the required torque drops dramatically and the blade efficiency increases as shown in Figure 19.

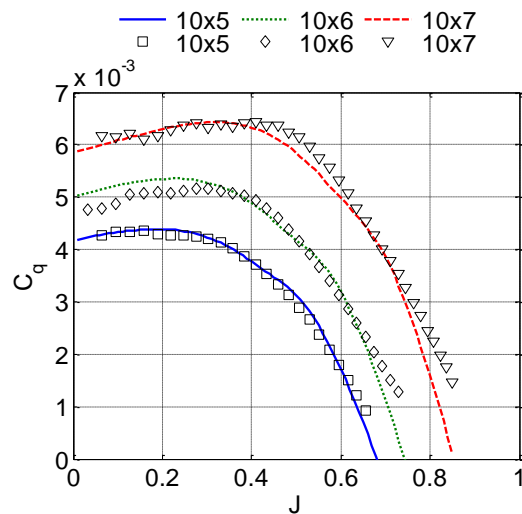


Figure 17: Analytic and experimental torque coefficients for the APC 10x5, 10x6, and 10x7.

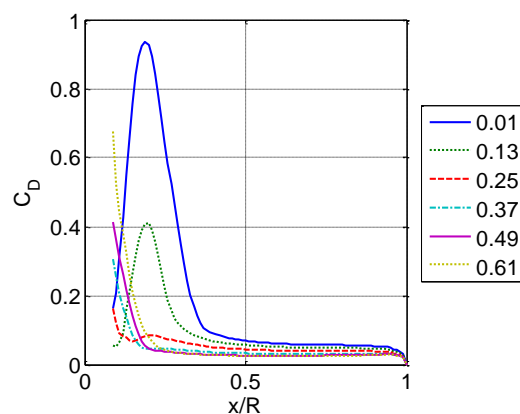


Figure 18: C_D versus spanwise location for different advance ratios for APC 10x5.

The overall propulsive efficiency is shown in Figure 19. From this figure, the experimental measurements closely match the predicted performance provided by the BEM. The discrepancies are largely attributed to experimental uncertainty created by vibrations in the experimental apparatus. Table 2 summarizes the experimentally determined advance per revolution. From these results, the model and the experimental data are in close agreement. The manufacturer's reported advance is lower in all cases which is consistent with other investigations of similar propellers.^{5,6}

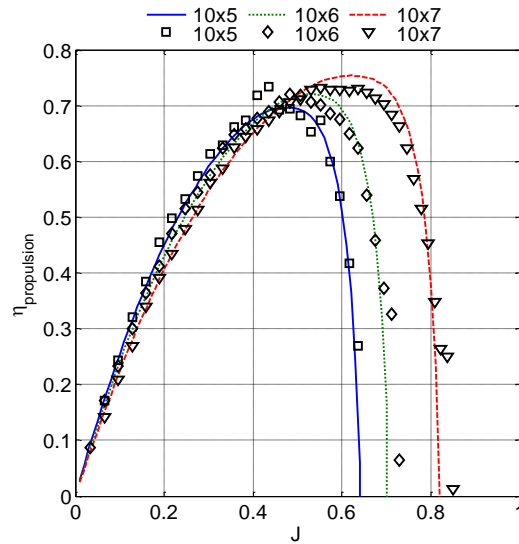


Figure 19: Analytic and experimental propulsive efficiency for the APC 10×5, 10×6, and 10×7.

Table 2: Analytic advance ratio

Propeller	Published Advance/rev (inches)	Analytic Advance/rev (inches)	Experimental Advance/rev (inches)	Percent Difference Pub./Ana.	Percent Difference Pub./Exp.	Percent Difference Ana./Exp.
APC 10×5	5	6.4	6.5	28%	30%	1.5%
APC 10×6	6	7.2	7.4	20%	23%	2.7%
APC 10×7	7	7.9	8.2	13%	17%	3.8%

D. Reynolds Performance

The variation in performance over a range of Reynolds numbers was measured by Brandt and Selig.⁵ In their work, the propeller RPM was held constant and the efficiency versus advance ratio was measured. As the Reynolds number is reduced, the overall propulsive efficiency decreases. From these tests, it was concluded that there are significant Reynolds based effects that are not typically encountered on larger scale, and higher power propellers. A reduction in local Reynolds number typically results in a decreased L/D for a given angle of attack. The reduced L/D translates to lower thrust for a similar power input. The lift and drag variation with respect to different Reynolds numbers has been well documented in various works.²⁰⁻²²

For the present work, the BEM model was used to predict the performance of propellers at varying Reynolds numbers. The inclusion of the BEM model is critical to this effort as the local variation in spanwise Reynolds number is appreciable on the scale of the propellers tested. The predictions generated by the BEM model are then compared to wind tunnel measurements using the same experimental apparatus as the full power tests outlined in the previous sections.

Testing the propellers at a constant Reynolds number requires reducing the RPM of the propeller while increasing the tunnel speed. The tunnel/propeller control is complicated by the fact that the propeller induces significant velocities in the tunnel, complicating the design of the wind tunnel controller. The propeller Reynolds number is evaluated at 75% of the span in a similar fashion to the mean force coefficients. The tunnel controller uses LabVIEW and a standalone Parallax Propeller RPM and throttle controller. Using these devices, the local chord Reynolds number was held to within 3% of the static thrust Reynolds number over the positive thrust advance ratio range. Figure 20 shows the Reynolds number variation for the APC 10×5 during a constant- Re test.

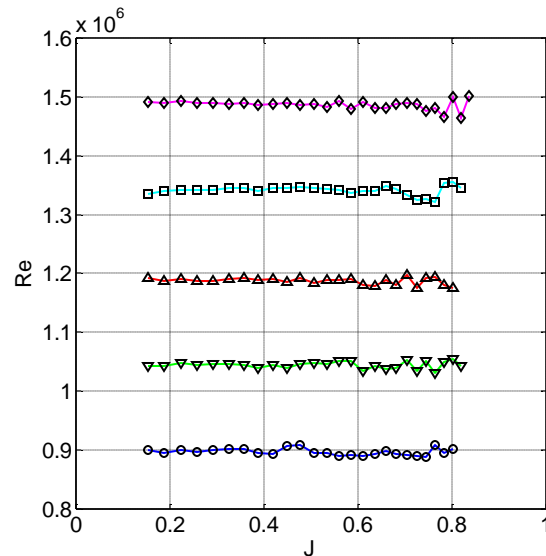


Figure 20: Reynolds number measured at 75% of the blade span for the APC 10x5. Different lines indicate different test set points.

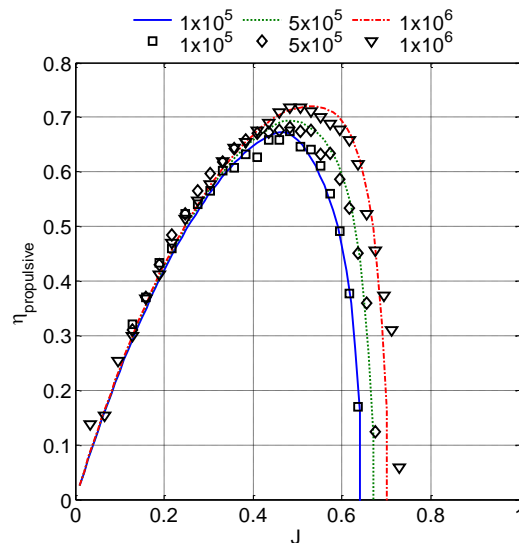


Figure 21: Analytic and experimental propulsive efficiency for APC 10x5 at varying Reynolds numbers.

Figure 21 shows the variation in propulsive efficiency for the APC 10x5 with different Reynolds numbers. For low advance ratios, the overall trending is unaffected by the change in Re . An appreciable drop in efficiency occurs at the maximum advance ratio. The drop in efficiency is related to the increase in drag and decrease in lift occurring at lower Reynolds numbers. Lift and drag coefficients for the NACA 4412 corresponding to the Reynolds ranges tested are shown in Figure 22. From this figure, the lift and drag change dramatically over a relatively small Reynolds number range leading to the marked change in propeller performance. The analysis of the Reynolds effects is somewhat complicated by the spanwise variation in velocity. The spanwise variation of the lift and drag coefficients makes an analytic first order model for propeller performance prohibitively complex.

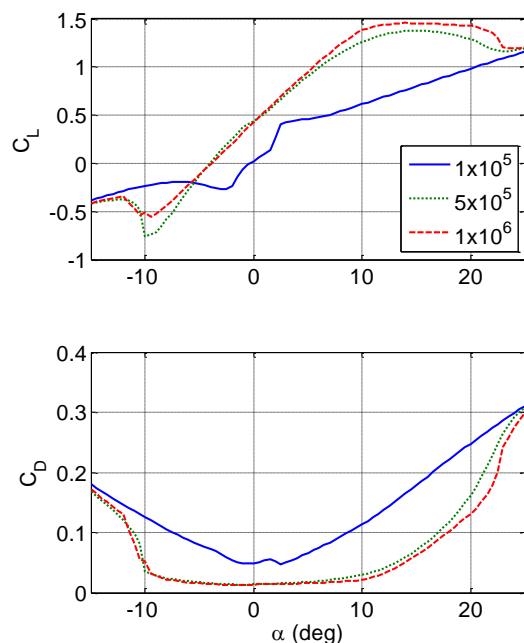


Figure 22: C_L and C_D for the NACA 4412 for three Reynolds numbers bounding the experimental data.

The performance difference at the three representative Reynolds numbers can be explained by a spanwise variation in aerodynamic characteristics. For the constant Reynolds number tests, the ratio of the freestream velocity and rotational velocity remains constant. Therefore, the angle of attack is relatively constant between Reynolds cases. Subtle variations are present due to the induced velocity components that change as a function of the local lift and drag coefficients. Figure 23 shows the BEM predicted angle of attack for the three Reynolds number test cases at the same advance ratio. Although the angle of attack changes very little with Reynolds number, the lift and drag coefficients results vary significantly with Reynolds as shown in Figure 24.

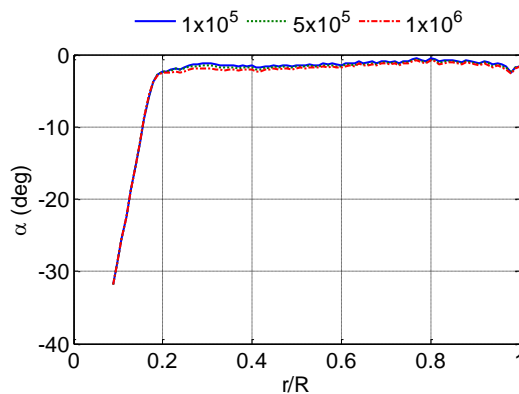


Figure 23: Spanwise angle of attack variation for the APC 10x5 at $J = 0.55$.

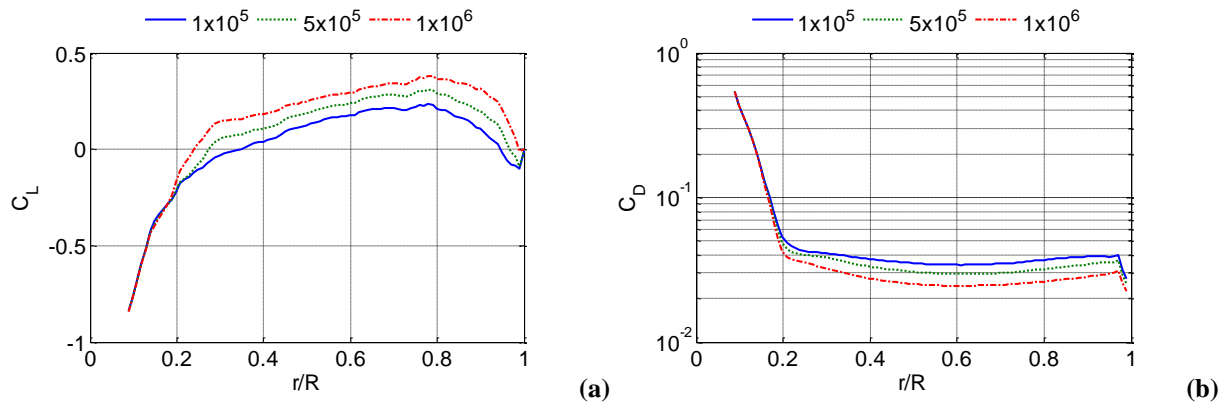


Figure 24: Spanwise C_L (a) and C_D (b) variation for the APC 10x5 at $J = 0.55$.

E. System Efficiency

The final characterized component is the power system's electrical efficiency. The electrical efficiency term allows for the correlation between measured electrical power and propulsive efficiency. The electrical efficiency is given as the ratio of motor and applied electrical power. This encompasses the power delivery system and motor mechanical efficiency. Typical efficiencies for the power system components range from 70 to 90% and depend on operating temperature and electrical load.⁶ The battery represents another efficiency term, but as the power is measured downstream, it does not impact the overall system efficiency.

Figure 25 shows the electrical efficiency for the three representative propellers tested at full power. This figure shows an appreciable and non-linear variation in electrical efficiency parameterized by advance ratio. To utilize this data in a predictive model, a surface fit is necessary. From Figure 25, approaching the full power design advance, the electrical efficiency decreases by up to 10%. The efficiency decrease is caused by a dramatic reduction in drag, and therefore power required. The speed controller's efficiency decreases at high angular speeds and low power output, likely due to internal switching inefficiencies and timing delays. The variation in electrical efficiency versus Reynolds number shows similar trending, as shown in Figure 26. At low Reynolds numbers, the efficiency decreases as the advance ratio approaches the design advance. As the Reynolds number increases, the efficiency at low advance ratios plateaus before sharply decreasing close to the design advance. The trending is monotonic and similar between propellers operating at the same Reynolds number. The similarity in trending allows for the generation of a parameterized surface fit. Figure 27 shows an example of the surface fit for the electrical efficiency versus advance ratio. From this plot, the monotonic trending is fit by a third order polynomial surface. The electrical efficiency is combined with the propulsive efficiency to determine the overall system efficiency as a function of Reynolds number and advance ratio. The surface fit, shown in Figure 27, allows for inflight estimation of the power available based on measured airspeed, electrical power, and propeller rotation speed. The parameterized surface fit is a critical component necessary for future vehicle performance estimation.

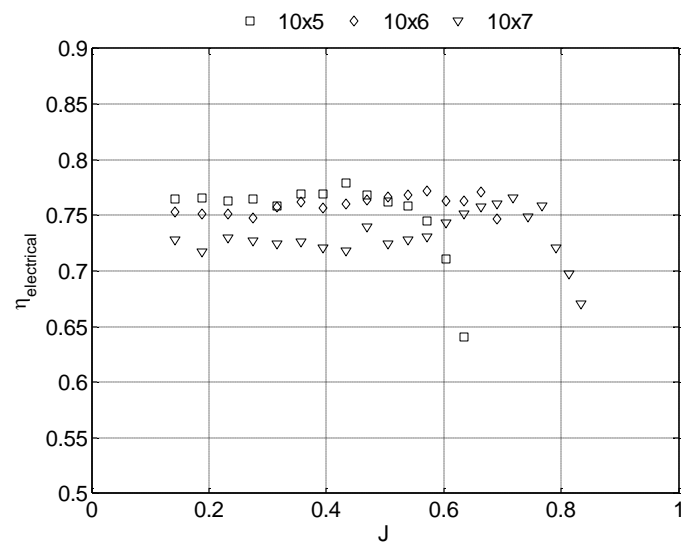


Figure 25: Electrical efficiency for the APC 10x5, 10x6, and 10x7 tested at full power.

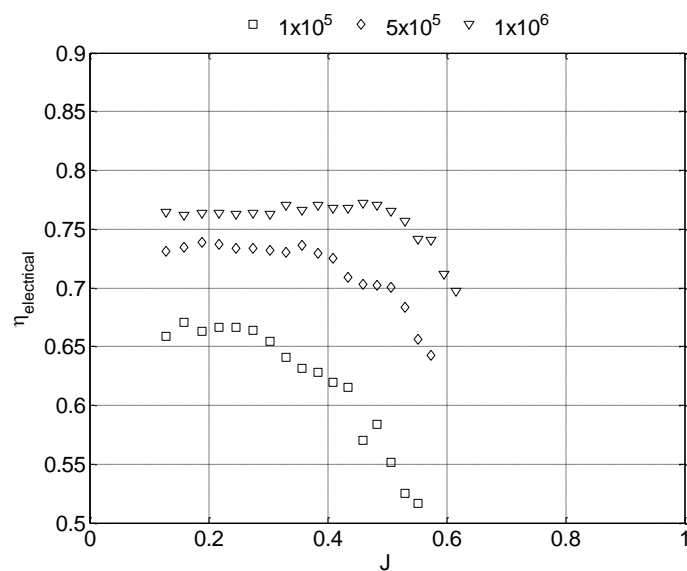


Figure 26: Electrical efficiency for the APC 10x6 at different Reynolds numbers.

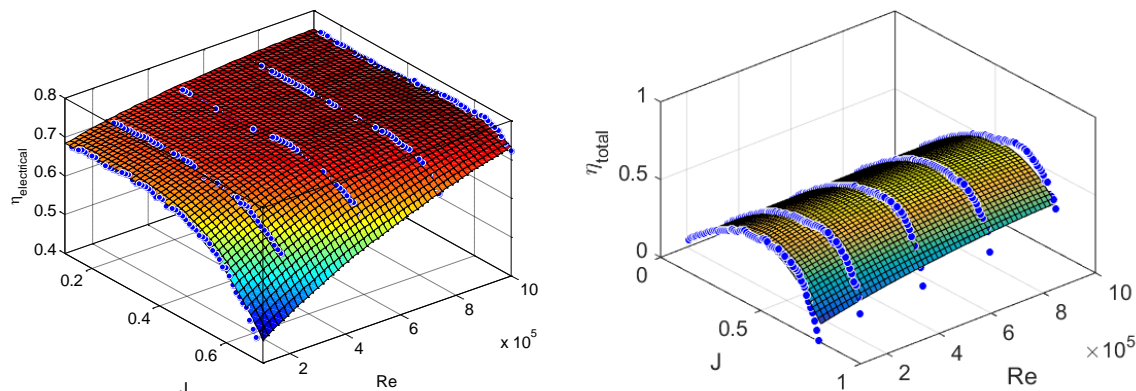


Figure 27: Surface fit of electrical efficiency versus Re and J (left) and the total system efficiency versus Re and J for the APC 10 \times 6.

V. Conclusion

A BEM model is presented and used for performance predictions on small-scale UAS propellers. Several corrections were proposed to the BEM model to capture features unique to the rotational flow around finite low-Reynolds number bodies. Namely, the use of an XFOIL-generated aerodynamic database, tip loss corrections, Mach corrections, and the incorporation of spanwise flow components were added to the model. For the specific propeller geometries considered in this work, the BEM predictions follow the general trends expected for fixed pitch propellers.

The BEM model was validated by a series of wind tunnel tests. From these tests, favorable comparisons between the predicted and measured theoretical advance were noted. Full power testing yielded results similar to those published in previous studies of small scale propellers. A novel constant Reynolds number test was presented to demonstrate the effects of scale on the propulsive efficiency. The favorable comparison between experimental- and model-based performance metrics such as propulsive efficiency and thrust/power coefficients point towards the importance of incorporating Reynolds dependency in the analysis of a small scale propulsion systems. The methodology for determining the performance of the remaining individual propulsion components such as the motor and electronic speed controller were presented. Using these estimates, the total system efficiency was determined. These estimates allow for a direct correlation between measured electrical power, advance ratio, and propulsive efficiency. From the propulsive efficiency, the thrust and power available can be estimated. Ultimately, the power available models enable high fidelity vehicle performance estimates for small scale UASs.

References

1. Madsen, H.A., Mikkelsen, R., and Øye, S., "A Detailed investigation of the Blade Element Momentum (BEM) model based on analytical and numerical results and proposal for modifications of the BEM model," *Journal of Physics: Conference Series*, Vol. 75, 012016, 2007. doi: [10.1088/1742-6596/75/1/012016](https://doi.org/10.1088/1742-6596/75/1/012016).
2. Merrill, R.S., "Nonlinear Aerodynamic Corrections to Blade Element Momentum Model with Validation Experiments," M.S. Thesis, *All Graduate Plan B and other Reports*, Paper 67, Utah State University, 2011. <http://digitalcommons.usu.edu/gradreports/67>
3. Snel, H., Houwink, R., and Bosschers, J., "Sectional prediction of lift coefficients on rotating wind turbine blades in stall," ECN-C-93-052, Energyresearch Centre of the Netherlands (ECN), Petten, the Netherlands, December 1994. <ftp://ftp.ecn.nl/pub/www/library/report/1993/c93052.pdf>
4. Uhlig, D.V. and Selig, M.S., "Post Stall Propeller Behavior at Low Reynolds Numbers," AIAA 2008-0407, 46th AIAA Aerospace Sciences Meeting and Exhibit, Reno, NV, January 7-10, 2008. doi: [10.2514/6.2008-407](https://doi.org/10.2514/6.2008-407)
5. Brandt, J.B. and Selig, M.S., "Propeller Performance Data at Low Reynolds Numbers," AIAA 2011-1255, 49th AIAA Aerospace Sciences Meeting including the New Horizons Forum and Aerospace Exposition, Orlando, FL, January 4-7, 2011. doi: [10.2514/6.2011-1255](https://doi.org/10.2514/6.2011-1255)

6. Brezina, A.J. and Thomas, S.K., "Measurement of Static and Dynamic Performance Characteristics of Electric Propulsion Systems," AIAA 2013-0500, 51st AIAA Aerospace Sciences Meeting including the New Horizons Forum and Aerospace Exposition, Grapevine, TX, January 7-10, 2013. doi: [10.2514/6.2013-500](https://doi.org/10.2514/6.2013-500)
7. Gamble, D.E. and Arena, A., "Automated Dynamic Propeller Testing at Low Reynolds Numbers," AIAA 2010-0853, 48th AIAA Aerospace Sciences Meeting Including the New Horizons Forum and Aerospace Exposition, Orlando, FL, January 4-7, 2010. doi: [10.2514/6.2010-853](https://doi.org/10.2514/6.2010-853)
8. Leishman, J.G., *Principles of Helicopter Aerodynamics*, 2nd ed., Cambridge University Press, Cambridge, UK, 2006.
9. Hansen, M.O.L., *Aerodynamics of Wind Turbines: Rotors, Loads and Structure*, James & James Science Publishers, London, UK, 2000, pp. 48-59.
10. Shen, W.Z., Mikkelsen, R., Sørensen, J.N., and "Tip loss corrections for wind turbine computations," *Wind Energy*, Vol. 8, No. 4, 2005, pp. 457-475. doi: [10.1002/we.153](https://doi.org/10.1002/we.153)
11. Lindenburg, C., "Investigation into rotor blade aerodynamics," ECN-C-03-025, Energyresearch Centre of the Netherlands (ECN), Petten, the Netherlands, July 2003, [ftp://ftp.ecn.nl/pub/www/library/report/2003/c03025.pdf](http://ftp.ecn.nl/pub/www/library/report/2003/c03025.pdf)
12. Liu, S. and Janajreh, I., "Development and application of an improved blade element momentum method model on horizontal axis wind turbines," *International Journal of Energy and Environmental Engineering*, Vol. 3, No. 1, December 2012, article 30. doi: [10.1186/2251-6832-3-30](https://doi.org/10.1186/2251-6832-3-30)
13. Ostowari, C. and Naik, D., "Post-stall wind tunnel data for NACA 44xx series airfoil sections," SERI/STR-217-2559, Solar Energy Research Institute, Golden, CO, January 1985. doi: [10.2172/5791328](https://doi.org/10.2172/5791328)
14. Drela, M., "XFOIL: An analysis and design system for low Reynolds number airfoils," *Low Reynolds Number Aerodynamics*, Mueller, TJ, ed., *Lecture Notes in Engineering*, vol. 54, Springer, Berlin, 1989, pp. 1-12. doi: [10.1007/978-3-642-84010-4_1](https://doi.org/10.1007/978-3-642-84010-4_1)
15. Tangler, J.L. and Kocurek, J.D., "Wind Turbine Post-Stall Airfoil Performance Characteristics Guidelines for Blade-Element Momentum Methods," AIAA 2005-0591, 43rd AIAA Aerospace Sciences Meeting and Exhibit, Reno, NV, January 10-13, 2005. doi: [10.2514/6.2005-591](https://doi.org/10.2514/6.2005-591)
16. Sequeira, C.J., Willis, D.J., and Peraire, J., "Comparing Aerodynamic Models for Numerical Simulation of Dynamics and Control of Aircraft," AIAA 2006-1254, 44th AIAA Aerospace Sciences Meeting and Exhibit, Reno, NV, January 9-12, 2006. doi: [10.2514/6.2006-1254](https://doi.org/10.2514/6.2006-1254)
17. Barnitsas, M.M., Ray, D., and Kinley, P., "Kt, Kq and Efficiency Curves for the Wageningen B-Series Propellers," Department of Naval Architecture and Marine Engineering, College of Engineering, The University of Michigan, Report No. 237, May 1981. <http://hdl.handle.net/2027.42/3557>
18. Corrigan, E.K. and Altman, A., "Survey of Small Unmanned Aerial Vehicle Electric Propulsion Systems," AIAA 2008-0179, 46th AIAA Aerospace Sciences Meeting, Reno, NV, January 7-10, 2008. doi: [10.2514/6.2008-179](https://doi.org/10.2514/6.2008-179)
19. Barlow, J.B., Rae, W.H., Jr., and Pope, A., *Low-speed wind tunnel testing*, 3rd ed., John Wiley & Sons, New York, 1999.
20. Shyy, W., Lian, Y., Tang, J., Viiaru, D., and Liu, H., *Aerodynamics of Low Reynolds Number Flyers*, Cambridge University Press, Cambridge, UK, 2008.
21. Hoerner, S.F. and Borst, H. V., *Fluid-Dynamic Lift: Practical Information on Aerodynamic and Hydrodynamic Lift*, Hoerner Fluid Dynamics, Bakersfield, CA, 1992.
22. Kothari, A.P. and Anderson, J.D., "Low Reynolds Number Effects on Subsonic Compressibility Corrections," *Journal of Aircraft*, Vol. 24, No. 8, 1987, pp. 567-568. doi: [10.2514/3.45477](https://doi.org/10.2514/3.45477)